1 # Multiscale light-sheet organoid imaging framework

2 Gustavo de Medeiros[1], Raphael Ortiz[1,2], Petr Strnad[1,3], Andrea Boni[1,3], Franziska Moos[1], Nicole

3 Repina[1], Ludivine Chalet Meylan[1], Francisca Maurer[1] and Prisca Liberali[1,4,*]

4 [1] Friedrich Miescher Institute for Biomedical Research (FMI) Maulbeerstrasse 66, 4058 Basel.

5 [2]Current address: Disney Research Studios, Stampfenbachstrasse 48, 8006 Zürich

6 [3]Current address: Viventis Microscopy Sàrl, EPFL Innovation Park, Building C, 1015 Lausanne.

7 [4]University of Basel, Basel, Switzerland

8 *Correspondence should be addressed to P.L. (prisca.liberali@fmi.ch)
9

10

11 # Abstract

12 Organoids provide an accessible *in-vitro* system to mimic the dynamics of tissue regeneration
13 and development. However, long-term live-imaging of organoids remains challenging. Here
14 we present an experimental and image-processing framework capable of turning long-term
15 light-sheet imaging of intestinal organoids into digital organoids. The framework combines
16 specific imaging optimization combined with data processing via deep learning techniques to
17 segment single organoids, their lumen, cells and nuclei in 3D over long periods of time. By
18 linking lineage trees with corresponding 3D segmentation meshes for each organoid, the
19 extracted information is visualized using a web-based "Digital Organoid Viewer" tool allowing
20 unique understanding of the multivariate and multiscale data. We also show backtracking of
21 cells of interest, providing detailed information about their history within entire organoid
22 contexts. Furthermore, we show cytokinesis failure of regenerative cells and that these cells
23 never reside in the intestinal crypt, hinting at a tissue scale control on cellular fidelity.

24

25 # Introduction

26 During adult life, organs such as the intestine are challenged to diverse environmental
27 conditions, requiring the tissue to be robust and yet plastic. For instance, during regeneration
28 after damage, surviving cells need to carefully orchestrate a fast and robust regrowth process
29 in coordination with proper shape recovery as well as functional and morphological
30 remodeling. To best overcome the difficulties surrounding the study of these tissue dynamics
31 in inner organs *in vivo*, organoids have become a powerful experimental method owing to
32 their exceptional accessibility and manipulability[1-3]. For the case of the intestinal tract,
33 intestinal organoids grown from single cells functionally recapitulate both the regenerative
34 response of the intestinal epithelium as well as the homeostasis of the *in vivo* intestine[4].
35 Morphologically, they also recapitulate the main dynamics of crypt formation, making them
36 a unique *in vitro* system[5,6,7,8].

Although with high degree of accessibility, performing live imaging of organoid growth remains a challenge, as it typically requires not only microscopy techniques capable of stable long-term imaging of several samples simultaneously, but also dedicated analysis and processing pipelines that can cope with complex imaging data. On the more technical imaging side, high-resolution multi-view light-sheet imaging has been used to track single cells in different embryo development settings [9,10], at the cost of low throughput imaging (usually 1-5 samples per imaging experiment). This is detrimental since the efficiency of organoid formation from single cells is particularly low (around 15% in the case of murine intestinal organoids[6]). Furthermore, previous work on the live recording of organoid dynamics has focused either on specific biological questions[6,8,11], organoid wide phenotype-driven screening approaches[12-14], or on specific isolated tools[15] without a more generalised yet in-depth approach on light-sheet imaging and data analysis. In another work which aimed at creating a light-sheet organoid imaging platform[16] the focus was mainly on the determination of culture-wide heterogeneities through a combination of both light-sheet and wide-field techniques. Although showing organoid diversity within the same culture, in-depth cellular multi-scale analysis for each organoid remained lacking.

To bridge the gap and provide quantitative information on organoid growth dynamics with in-depth cellular analysis, we here provide a unified multiscale light-sheet imaging framework tailored to live organoid imaging. Our framework incorporates optimized imaging, pre-processing, semi-automated lineage tracking, segmentation and multivariate feature extraction pipelines which provide multiscale measurements from organoid to single cell levels. By focusing on the development of intestinal organoids, we show that this holistic set of tools allows the combination of whole organoid and single cell features to be analysed simultaneously, having both lineage tree as well as spatial segmentation information presented in a clear and unified way. We demonstrate that our pipeline is compatible with fixation and immunolabeling after live imaging by tracking back cells positive for specific markers and compare the history of these cells with all other cells in the organoid. To facilitate the usage of the analysis and visualization tools, we have combined them into a unified set of tools we call LSTree[17], built on a Luigi workflow and dedicated notebooks, allowing the different steps to run in a modular way. Further, we use our framework to dissect previously unknown biological insights on the role of polyploidy during intestinal organoid growth, and we propose a tissue level check point for tissue integrity that could start explaining the interplay between regeneration and cancer.

Results

Imaging framework for light-sheet microscopy of organoid growth

We developed a multiscale imaging framework that comprehends acquisition, pre-processing, automated tracking, segmentation with further feature extraction as well as visualization dedicated for 3D live imaging (**Fig. 1a**). In this work, we applied our framework to live intestinal organoid light-sheet recordings performed with a dual-illumination inverted light-sheet[6] microscope, which utilizes a multi-positioning sample holder system (**Fig. 1b**). In order to image organoid development, we followed previously published protocols[6], FACS sorting single cells (**Supplementary Figure 1a**) from mature organoids and mounting them as

2

80 5 uL mix drops with Matrigel on top of a ca. 50 um thick fluorinated ethylene propylene (FEP)
81 foil, which are then covered in medium (**Fig 1c** left and **Methods Section**). To stabilize the
82 imaging, we patterned the FEP foil used for mounting in order to create small wells
83 (**Supplementary Figure 1b-d**, **Supplementary Note 1**), allowing better control of the sample
84 position within the holder, while improving reproducibility of experiments by preventing
85 drops from being washed away during medium change of fixation procedures. As previously
86 demonstrated, the microscope we utilized is capable of imaging live intestinal organoids for
87 long periods of time[6,8] , as well as acquiring time-lapses of mouse embryonic and gastruloid
88 development[18,19]. However, one important drawback of the system was that the alignment
89 of the illumination beams is done only once, prior to the experiment and irrespective of the
90 position of the sample in the dish or holder. Although sufficient in certain situations (e.g.
91 mouse embryo imaging), imaging of samples embedded and distributed inside a gel suffer
92 from refractive index mismatch between water and Matrigel, as well as from the presence of
93 other obstacles in the light-path (other organoids or debris) and from the curved shape of the
94 sample holder itself. Therefore, to improve recording conditions in every individual sample,
95 we developed a position dependent illumination alignment step. This allows to fine tune the
96 alignment of each of the illumination sheets in respect to the detection plane for every sample
97 position so that best image quality possible can be achieved throughout (**Fig 1b** right and
98 **Supplementary Note 1**).

99 To minimize storage needs and improve SNR, acquired images are cropped using a dedicated
100 tool that automatically corrects for 3D sample drifting (**Fig 1d** upper row). The cropped
101 images may also be further pre-processed through denoising and deconvolution steps.
102 Denoising is performed using the Noise2Void scheme[20], with its output sent to a tensor-flow
103 based image deconvolution[21] (**Fig 1d** lower row) using measured PSFs from beads
104 (**Supplementary Note 2** and **Methods Section**).

105 With these first modules at hand, we imaged organoids expressing Histone 2B and mem9
106 membrane peptide tagged with mCherry and GFP respectively, recording the growth and
107 development of several organoids starting from single cells or 4-cell spheres (**Fig 1e** and
108 **Supplementary Movie 1**) every 10 minutes throughout the course of around 4 days. The
109 collected data comprised of organoids that form both budding and enterocyst phenotypes:
110 whereas budding organoids grow from single cells into mature organoids with both crypt and
111 villus structures, enterocysts, comprised of terminally differentiated enterocytes, do not have
112 crypts as they do not develop Paneth cells required for the establishment of the stem cell
113 niche, a necessary step for crypt formation[6,8].

114 For the analysis, we initially performed single-cell partial semi-automatic tracking using the
115 Fiji plugin Mastodon (https://github.com/mastodon-sc/mastodon) on 7 datasets. After that,
116 we extracted features based on organoid and single cell segmentation and plotted this data
117 over time (**Fig 1f** and **Supplementary Table 1**). For example, we noticed large variability in cell
118 division synchronicity, as in some datasets the nuclei number growth over time loses the
119 typical staircase-like behavior already early during the first day of recording. Although
120 epithelium volume growth curves follow that of nuclei number, with the characteristic
121 exponential behavior, nuclei density slightly increases over time. Mean cell volume showed
122 characteristic mitotic peaks, with overall cell volume decrease over time, matching the
123 increase in nuclei density. Interestingly, although initially cell to nuclei volume ratio vary, all
124 datasets converge to common steady state values where the cell volume is ca. 3 to 4 times
125 larger than the nuclear volume. We also observed a consistent change in organoid volume

3

126   due to medium change during the live recordings (**Supplementary Figure 2**). As this initial
127   assessment of our imaging data showed consistent and reproducible results, and to handle
128   larger dataset more rapidly and consistently, we developed an integrated and automated
129   approach to turn the imaging into digital organoids with a visualization tool.
130
131   Dedicated image processing workflow

132   To make the entire analysis and visualization tools directly accessible, we incorporated all
133   image processing and data analysis modules into a unified workflow named LSTree, having
134   most processing and training steps implemented using Luigi based tasks, and the rest as
135   jupyter notebooks for cropping and segmentation evaluation. The workflow along with
136   juypter notebook and two example datasets are provided as a documented Github repository
137   with step-by-step guide (see **Methods Section** and **Supplementary Notes 2-4** for more
138   information).

139   In the first pre-processing step, the user selects which organoid needs to be cropped. This
140   automatically generates minimal bounding boxes per time-point as well as global bounding
141   box (**Fig 2a**). The workflow also has an interactive tool to review the crops and perform few
142   manual corrections, e.g. to account for large displacement between consecutive frames
143   (**Supplementary Figure 3**). Next, if needed, denoising and deconvolution of cropped and
144   registered movies is performed as one combined step. Important to note that we chose to
145   denoise and deconvolved our datasets as the image quality usually decays quite heavily at
146   later timepoints. However, this is not a requirement, and the prediction models can also be
147   trained based on good quality unprocessed datasets. More details on how to bypass the
148   denoising and deconvolution steps are discussed through the example datasets provided in
149   the GitHub documentation.

150   For the segmentation of organoids, as well as their cells and nuclei, we adopted different
151   segmentation strategies all relying on existing convolutional neural networks (**Fig 2b**). Our
152   main initial motivation was to test whether we could incorporate the spatial information from
153   the lineage trees spots for training segmentation models. To that end, we decided to use the
154   RDCNet instance segmentation network as a base[22], taking advantage of its inherent recursive
155   architecture. First, nuclei are segmented in 3D following a deep learning model trained with
156   a mix of complete and partial annotations. A small subset of the frames is fully annotated by
157   manually expanding the labels to the full nuclei, whereas partial annotations rely on the initial
158   tracking performed with Mastodon by drawing spheres at the position of tracked nuclei. (**Fig
159   2b** upper row). Jupyter notebooks for interactive visualization and correction of the predicted
160   segmentation are also part of the framework and added onto the GitHub, which allows
161   improving the model accuracy with minimal annotating time. To check whether this approach
162   was valid, we compared the trained network output with randomly selected hand-annotated
163   image volumes, yielding very good results (see **Supplementary Note 5** and **Supplementary
164   Figure 4a-b**).

165   Motivated by the initial results with nuclei segmentation based on sparse annotations, we
166   took a similar approach for cell segmentation. To this end, organoid and cell segmentation
167   also use RDCNet and leverages the pre-computed nuclei segmentation to avoid manual
168   annotations of individual cells. At the same time, we added a constraint based on lumen and
169   epithelium segmentation, to avoid that cell labels spread outside of the epithelial layer. To
170   subdivide the epithelium mask into cells, the previously segmented nuclei are used as partial

4

171   cell annotations under the assumption that they are randomly distributed within the cell
172   compartment (**Fig 2b** lower row, **Supplementary Note 3**). Finally, in addition to the
173   segmentation volumes and nuclei number (**Fig. 1e**), several different features are extracted
174   such as nuclear distance to apical/basal membranes, fluorescence intensity, distance to
175   parent node and number of neighbors per cell (For a complete list of features with short
176   explanations see **Supplementary Table 1**).

177

178   ## Deep learning model for automated lineage tracing

179   Although suitable for estimating lineage trees for few datasets, semi-automated tracking of
180   many datasets with the Mastodon Fiji plugin can be time consuming, as different datasets
181   may require different setting parameters often break when cells are too packed or with low
182   signal-to-noise. To significantly improve this process, we trained and refined a deep learning
183   model on the available tracked datasets aiming at automatic generation of candidate trees
184   that only require minimal corrections (**Fig 2c,d, Supplementary Note 3**). To avoid usage of
185   tracing algorithms that enforce a complex set of rules[23-25], we developed a joint
186   segmentation-tracking approach that simultaneously predicts matching nuclei labels on 2
187   consecutive frames. To this end, we extended the RDCNet instance segmentation model to
188   predict pseudo 4D labels (3D convolutional network with time axis as an additional image
189   channels) mapping correspondences between nuclei in 2 consecutive frames (**Fig 2c**).
190   Predicting linked nuclei segmentations has the advantage to enforce constancy over the
191   entire nuclear volume rather than relying on an ambiguous center, as well as implicitly
192   enforcing rules such as minimum cell distance or plausible nuclei volume constraints in a data-
193   driven manner. This method keeps the number of manual hyper-parameters tuning to a
194   minimum and can be improved over time as more validated and corrected datasets are
195   incorporated in the training set. In a complementary manner, this method can be used
196   together with other deep learning strategies such as Elephant in a complementary and
197   modular manner, in which curated trees via Elephant can be used for training of more
198   generalized tracking models based on RDCNet, or even directly used for nuclei/cell
199   segmentation training/prediction.

200   To assemble the predicted tree in the framework, nuclei labels in each frame are connected
201   to their parents in the previous frame by finding the linking label with the maximum overlap
202   (**Fig 2c, Supplementary Figure 5**). The predicted tree is then saved with the structure of a
203   MaMuT.xml track file, which can be then imported into Mastodon for further correction if
204   necessary (**Fig 2d**). As a direct consequence of the joint segmentation, additional information,
205   such as the nuclei volume, can be overlaid on the predicted trees to aid in the curation process
206   (**Supplementary Figure 5**, Supplementary **Note 3**). For instance, jumps in nuclear volume
207   highlight positions where tracks should be merged or split. The manual curation time ranges
208   from minutes to a couple hours on the most challenging datasets (e.g. low SNR images,
209   abnormal nuclei shape). In summary, the here developed lineage tree prediction approach
210   allows high quality prediction of intestinal organoid lineage trees with long tracks spanning
211   multiple division cycles (up to 5 generations in this work) enabling tracked data to cross
212   spatiotemporal scales. To further challenge our tracking prediction strategy, we have also
213   tested it outside of our main focus on live imaging of intestinal organoid, and used trained
214   models to validate prediction accuracy on mouse embryo datasets from published work
215   (**Supplementary Figure 4c-e,** and discussions on **Supplementary Note 5**), also comparing it to

216 output from trained Elephant Tracker models (all trained models can be found in the
217 **Supplementary Software**).

218

Digital organoid viewer

220 With the lineage trees and the deep learning 4D segmentation of organoid, lumen, cells and
221 nuclei at hand, we developed a multiscale digital organoid viewer to explore and perform in-
222 depth data mining. The viewer combines both lineage trees and segmented meshes,
223 facilitating the direct comparison of different features within a multiscale digital organoid
224 framework. We have added it to our LSTree Github repository along with example data, also
225 including the possibility to overlay recorded images with the corresponding meshes allowing
226 a direct inspection of the predicted segmentation (**Fig 3a, Supplementary Movie 2**). As can
227 be seen through the example datasets present in the repository, this interactive viewer allows
228 associated features to be displayed, selected nodes to be interactively highlighted on the
229 meshes, and color coding of both trees and meshes to be be assigned independently. This
230 way same or complementary features can be visualized at once (All currently extracted
231 features are discussed in **Supplementary Note 4** and **Supplementary Table 2**)

232 As an example of the image-analysis and visualization tools presented in the framework,
233 nuclear volume quantifications can be evaluated directly onto the tree of a specific dataset
234 (**Fig 3b**). Using this approach, it is possible to observe and quantify how much nuclei volumes
235 change with each generation and over time, with the smallest volumes observed right after
236 division. Similarly, we observe that the nuclear distance to the basal membrane (**Fig 3c**)
237 increases due to interkinetic nuclear migration towards the apical side. Combining the same
238 visualization procedure with the segmented meshes, we render the nuclei or cells in 3D, using
239 the same color-coding as for feature on the trees (**Fig 3d**). Last but not least, we also compare
240 the extracted features against the general trend from all other datasets combined, allowing
241 us a direct evaluation of variability across experiments (**Fig 3e,f**), evaluating the increased
242 distancing of nuclei from the apical membrane, a known effect due to epithelial polarization
243 (**Fig 3f**).

244 In summary, this is a unique set of tools embedded under the same workflow which allows
245 not only multiscale segmentation of organoids along with lineage tree predictions, but also
246 the simultaneous visualization of both trees and segmented meshes into a unified web-
247 viewer. All steps of the process are implemented to keep storage, memory, and manual
248 tuning requirements to a minimum, making this a powerful and yet easily accessible part of
249 the light-sheet framework.

250

Functional imaging through fixation and backtracking

252 Next, we analyzed functional information on the tracked cells and organoids contained in the
253 lineage trees. Although our imaging framework allows the visualization and quantification of
254 a large number of features at the cellular and organoid levels throughout organoid growth,
255 functional information remains dependent on fluorescent reporter organoid lines. The easiest
256 way to theoretically approach this is to perform stable multicolor live imaging for long periods
257 of time. However, overlapping emission/excitation spectra limits the total number of
258 fluorescent reporters and concerns regarding interference with the normal cell function,
259 signal-to-noise sensitivity for low abundant proteins, photostability and general phototoxicity

260   due to laser illumination limit the use of fluorescent reporters. To overcome this, we fixed
261   and added an immunolabelling steps at the end of the live recordings to assess the end state
262   of the cells. Then we tracked the immunolabelled cells back through the lineage tree (**Fig 4a**),
263   using LSTree for further visualization and analysis.

264   In details, we fixed the sample at the end of the recording with 4% PFA, to then perform the
265   immunolabelling protocol (see **Methods Section**). The pre-patterning of the FEP foil holding
266   the sample was crucial, as without it the Matrigel drops were washed out. To account for
267   organoid drifts, we imaged the entire fixation procedure, so that the organoids could be
268   tracked during fixation, leading to a recovery of more than 80% (for more detailed
269   information please see **Supplementary Note 6**). To register the fixed organoids to the last
270   time-point of the live recording we used similarity transformations implemented in ITK and
271   available via Elastix[28,29] (used as a stand-alone tool, as exemplified in **Fig 4b**. For more
272   information, please refer to the **Methods Section** and **Supplementary Note 6**). To test this
273   approach, we imaged H2B-mCherry, mem9-GFP organoids until day 3 (**Supplementary Movie
274   3** left). It has been shown that between around day 1.5 intestinal organoids break symmetry
275   through the appearance of the first differentiated cells of the secretory lineage (Paneth cells,
276   Lysozyme). Preceding the appearance of Paneth cells there is the local establishment of a
277   Notch-Delta lateral inhibition event, with future Paneth cells being typically Delta Like Ligand
278   1 positive (DLL1+)[6] . To analyze symmetry breaking, we fixed the organoids at 56 hours and
279   stained for DLL1-Alexa488 and Lys-Alexa647 (**Fig 4c-e-**, **Supplementary Movie 3** right).
280   Intriguingly, the two DLL1+ cells are two sister cells that were formed at the end of the division
281   from generation 5 to generation 6, around 10 hours before fixation.

282   To follow cellular dynamics and changes of features of these specific cells in their spatial
283   environment we analyzed nuclei and cell volumes (extracted with LSTree) per generation of
284   the backtracked cells from generation 5 and 6 and compared them to all the other cells during
285   the same generations (**Fig 4f**). Interestingly, cellular, and nuclear volumes of the backtracked
286   cells do not seem to deviate relative to each other during generation 5. After cell division and
287   entering generation 6, however, the nuclei volumes of both DLL1+ sister cells show an
288   increased relative difference to one another, with the Lys+ cell having a slightly larger nucleus.
289   Changes in nuclear volume related to appearance of DLL1+ signal was also observed in other
290   datasets (**Supplementary Figure 6**)**.**

291   Next, we evaluated the dynamics of neighbor exchange by cross-checking the closest cells to
292   a backtracked cell(s) of interest at each time-point with LSTree. We examined if the progeny
293   of these two sister cells had high level of mixing with other cells during cyst growth. From the
294   visualization of the tracked neighbors on the lineage tree and segmented meshes (**Fig 4g**), it
295   is apparent that neighbor exchanges, although distributed across the tree, do not happen
296   often nor with many different cells, keeping an average of 5 cells.

297   The above results show that, by combining our light-sheet framework with standard fixation
298   and registration techniques we can broaden the level of functional information, bridging it to
299   the dynamical processes during live imaging. Consequently, we were capable of dissecting
300   some initial dynamical elements preceding the formation of DLL1+ and Paneth cells in the
301   context of the entire organoid development, analyzing the process of symmetry-breaking
302   events across biological scales.

303

Nuclei merging events during organoid growth

From our backtracking example it became apparent that one cell undergoes multiple rounds of failed divisions, with two daughter cells merging before a new division starts (**Fig 5a**). Upon further inspection of the other lineage trees, we realized that most of the datasets contained at least one merging event during early phase of organoid growth whereby two sister nuclei, at the end of their cell cycle, divided again into two instead of into four nuclei (**Supplementary Figure 7**). To investigate whether a failed division during the previous mitotic cycle was causing these nuclei merging, we examined the last step of the previous cell division. In all cases there was a problem during late cytokinesis, with the two sister cells never fully separating (**Fig 5a,b**). Nuclear volume for all the daughters arising after the merging event is clearly increased and cell volume followed the same behavior, roughly doubling in tetraploid cells (**Fig 5c,d**). To dismiss the possibility that these mitotic failures are caused by phototoxic effects of the imaging itself, we performed a time-course experiment with wild-type organoids grown from single cells under same medium conditions as the live recordings. We fixed organoids at days 2 and 3, staining them for e-Cadherin and DAPI. Despite the lack of continuous illumination, the resulting data showed many cysts with polynucleated cells, as well as cells with enlarged nuclei (**Fig 5e**).

Using the framework we were able to follow the fate of the progeny of a cell that underwent cytokinesis failure and surprisingly we noticed that they can lead to cells that remain part of the epithelium until the end of the recordings without dying, when we can observe fully budded organoids or mature enterocysts (end of day 4) (**Fig 5f,g**). Yet, comparing to unaffected parts of the trees, this binucleation progeny typically has higher probability to be extruded into the lumen (~46% for merged progeny against ~5% for other cells). Another intriguing observation is that the remaining 54% of the cells are never localized to the crypt but to the villus (**Fig 5f**, **Supplementary Figure 8**). This is an interesting result, as it suggests that the cells that undergo cytokinesis failure, and might have chromosomal defect, do not migrate or differentiate into niche cells (Stem cells and Paneth cells) but stay as villus cells that are shorter lived. This might mean that there are mechanisms to maintain cellular integrity in the stem cell niche avoiding damaged cells in the crypt.

Molecularly, it is known that the Large tumor suppressor kinase 1 (Lats1) can influence cytokinesis failure via lack of inhibition of Lim kinase 1 (Limk1)[30-32]. This poses an interesting hypothesis on the role of mitotic failure in intestinal regeneration as Lats1 and Yap1 are master regulators of regenerative response of the intestinal epithelium[33,34]. Analysis of RNAseq from previous studies[6], show decrease in Lats1 expression during initial days of organoid growth that mimic the regenerative response of the intestinal epithelium[6]. This regenerative response is achieved by downregulating Lats1 as a negative regulator of Yap1. We initially stained for Limk1 and could see cell-to-cell variability of its expression (**Supplementary Figure 9a,b**). To further analyze the role of Lats1 and Limk1 in the regulation of cytokinesis failure in the early days of organoid formation we perturbed Lats1 and Limk1 activity. Time-course imaging of Lats1 double knockouts[6] showed several cysts with double nucleated cells that result from mitotic failures (**Supplementary Figure 9c**). Moreover, inhibition of Lats1 and Limk1 with chemical inhibitors (Truli and Damnacanthal, see **Methods Section** and **Supplementary Figure 9**), increased and decreased the number of bi-nucleated cells, respectively (**Fig 5h,i**). Lats1 inhibition also display an increase of Yap1 activation. This shows that in intestinal organoids formation, cytokinesis failure is regulated by Lats1 activity that in turn is a negative regulator of Limk1.

350 Taken together, through the multi scale approach of 3D segmentation, feature extraction and
351 lineage tree analysis we were able to identify consistent polyploidy events during early
352 intestinal organoid development and the fate of their progeny. Our framework allowed us to
353 bridge the observed mitotic defects across scales towards the tissue scale, showing the end
354 fate of the merged cells progeny and spatially locating them onto the mature organoid
355 morphology. This is shedding new light on the robustness of a regenerative YAP cellular state,
356 questioning the role of polyploidy in intestinal regeneration.

Discussion

358 Here we have presented a unified light-sheet imaging framework tailored to intestinal
359 organoid development. Our framework encompasses optimization of sample mounting,
360 microscope recording and pre-processing, generating high-quality datasets with minimal
361 storage needs. The image analysis and visualization part, named LSTree, is a comprehensive
362 approach that uniquely combines image pre-processing, single cell tracking and multiscale
363 segmentation and feature extraction along with a dedicated unified visualization and analysis
364 tool.   We show that this framework is capable of fully segmenting and tracking intestinal
365 organoids as they grow from single cells for several days, bridging biological scales to the point
366 when the organoid has hundreds of cells. Information on organoid, lumen, cell and nuclei
367 volumes along with other multivariate features can be simultaneously visualized with the
368 lineage tree data and further analyzed through a web-based Digital Organoid Viewer,
369 facilitating a more global understanding of the dynamics acquired at subcellular resolution.
370 The use of specialized neural networks dedicated to multiscale segmentation and lineage tree
371 predictions allow the framework to be plastic enough to handle different kinds of live-imaging
372 data as well as continuously improve through the utilization of dedicated tools for retraining
373 of the models. Furthermore, the training architectures keep the number of parameters and
374 computational resources to a minimum, relieving the needs for any highly specialized IT infra-
375 structure, as they can be directly used on off-the-shelf workstations.

376 The combination of live imaging with standard fixation techniques, via the development of
377 sample holder patterned with a cold stamp technique, allows the tracking of immunolabelled
378 cells back in time and space and compare their features to all of the other cells over the entire
379 organoid growth. Unlike lineage tracing in single cell RNA sequencing, which clusters cells by
380 their RNA phenotypic fingerprint or a barcode, with our approach we can focus on the missing
381 spatiotemporal organization in a causal way, as we follow the same cells over time.
382 Consequently, we can now address the evolution of cells that can give rise to the first
383 symmetry breaking event, keeping track of local interaction within the whole organoid.

384 Although suited to intestinal organoids, or to systems with smaller size, such as the mouse
385 embryo, we recognize that particular challenges can be addressed to make our framework
386 best suited to other case scenarios. For example, the application of our framework to larger
387 organoids (surpassing diameters of 200 μm or being composed of highly dense cell
388 aggregates) would best require light-sheet microscopes with more than one detection
389 objective, or with sample rotation, so that the samples can be visualized from the opposite
390 side as well, with the multi-view stacks properly fused afterwards. Furthermore, the
391 utilization of multiphoton imaging could be of benefit to improve light-tissue penetration

392 depth. Here the challenge is to provide multi-view imaging and yet keep the multi-sample
393 aspect, so that systems with low growth efficiency can also be studied.

394 On the analysis side, the utilization of tracking spots for aiding in nuclei segmentation
395 prediction shows to be an interesting approach to minimize the amount of hand annotated
396 data for training. The extension of this approach towards cell volume estimation is a valid first
397 approach, however, may still yield "noisy" cell volumes over time. To refine this, retraining
398 with a few hand-annotated cells would be of good practice. Lastly, lineage tree prediction is
399 still highly dependent on good temporal spacing and good nuclei segmentation. Especially for
400 the challenging case of samples with low efficiency, such as the intestinal organoids, we tackle
401 this issue with the careful adjustment of imaging parameters and of initial nuclei
402 segmentation, as well as by allowing the workflow to receive input from other tracking
403 methods such as Elephant. The possibility to use current state of the art tracking strategies
404 such as Elephant or Mastodon helps especially to get first lineage trees done, and allows our
405 LSTree workflow to be agnostic to only one approach. For the future we imagine that the
406 inclusion of 3D ellipsoids instead of only spheres as weak annotation input for nuclei
407 segmentation model training will aid in the nuclei segmentation quality, as the ellipsoids
408 inherently carry more spatial information on the shape of the nuclei to be segmented.

409 Last, we present appearance of cells having cytokinesis-related mitotic errors leading to
410 binucleation during early organoid growth. With LSTree we were able of rapidly verifying
411 these errors across a multitude of different long-term recordings, showing that they are a
412 consistent feature during early cyst growth. Interestingly, polyploidy has been associated with
413 wound healing after injury[36]. In the liver, polyploid cells seem to have a tumor-suppressor
414 role with polyploid cells occurring mostly due to cytokinesis failure and
415 endoreduplication[37,38]. However, polyploid hepatic cells are mostly quiescent and do not
416 divide unless the liver undergoes regenerative process due to a lesion. In contrast, our
417 observed bi-nucleated cells do not undergo cell cycle arrest, but continue to divide for even
418 multiple cycles, either with or without repeated clear mitotic failure. We also show that
419 although these cells may appear in the crypt region during crypt formation (during days 3-4),
420 they typically do not manage to reside in the crypt, whereas cells in the villus region remain
421 part of the epithelium. Mitotic errors are negatively regulated by overactivation of Lats1 via
422 regulation of Limk1. Since Lats has a direct implication during cytokinesis, we propose that
423 during organoid growth and possibly intestinal regeneration there must be a balance
424 between high-proliferative regenerative state – which is more error prone – and a
425 counteracting checkpoint at the tissue scale to avoid mutations in the stem cell compartment.
426 This way tissue integrity can be achieved fast, with any remaining mutations in the villus being
427 eventually shed off via e.g. anoikis when cells reenter homeostasis.

428 In conclusion, with LSTree we can cross biological scales with unprecedented detail, as we can
429 follow particular subcellular behaviors while keeping track on the entire tissue development
430 over long periods of time. The usability of the tools presented can go far beyond the examples
431 shown here, as they can be compatible with different light-sheet modalities making this
432 framework also very useful in the study of other 3D cell cultures. In particular for the analysis,
433 we believe LSTree to be a first step towards a comprehensive and quantitative framework
434 dedicated to the creation of fully digital organoid maps, so that the intrinsic culture
435 variabilities can be overcome with the creation of averaged organoids to be used as
436 landmarks for future studies.

437

Methods

438

Ethics statement

439

440 All animal based studies have been approved by Basel Cantonal Veterinary Authorities and
441 conducted in accordance with the Guide for Care and Use of Laboratory Animals.

442

Organoid lines

443

444 Male and female outbred mice between 8 and 12 weeks old were used for all experiments.
445 Regarding husbandry, all mice have a 12/12 hours day/night cycle. Medium temperature is
446 kept at 22°C and relative humidity at 50% .

447 Mouse lines used for time-course experiments: C57BL/6 wild type (Charles River
448 Laboratories), one 12 weeks old male and one 8 weeks female mice.

449 For all light-sheet movies, we used H2B-mCherry C57BL/6 x C3H F1 female intestines
450 heterozygous for H2B-mCherry (received already as intestines, kind gift from T. Hiragi lab,
451 EMBL). For H2B-mCherry/mem9-GFP organoids, H2B-mCherry organoids were infected with
452 LV.EF1.AcGFP1-Mem-9 lentivirus particle (Clontech, Takara Bio USA). For the H2B-miRFP670
453 line, B6/N x R26 Fucci2 (Tg/+) intestines (kind gift from J. Skotheim lab, Stanford) were
454 infected with pGK Dest H2B-miRFP670 (Addgene). For Lats DKO, Lats1Δ/Δ; Lats2Δ/Δ (LATS
455 DKO, intestines as kind gift from Jeff Wrana, Department of Molecular Genetics, University of
456 Toronto, Canada)[39] time-course of published data[6] was analyzed.

457

Organoid culture

458

459 For initial organoid culture a section of the initial part of the small intestine was opened
460 lengthwise and cleaned with cold PBS. Then, after removal of villi by scraping with a cold glass
461 slide, the section was sliced into small fragments of roughly 2 mm in length. All fragments
462 were then incubated in 2.5 mM EDTA/PBS at 4 °C for 30 min with shaking. Supernatant was
463 removed and pieces of intestine were re-suspended in DMEM/F12 with 0.1% BSA. The tissue
464 was then shaken vigorously. To collect the first fraction, the suspension was passed through
465 a 70 μm strainer.

466 The remaining tissue pieces were collected from the strainer and fresh DMEM/F12 with 0.1%
467 BSA was added, followed by vigorous shaking. The crypt fraction was again collected by
468 passing through a 70 μm strainer. In total, 4 fractions were collected. Each fraction was
469 centrifuged at 300g for 5 min at 4 °C. Supernatant was removed and the pellet was re-
470 suspended into Matrigel with medium (1:1 ratio) and plated into 24 well plates. Organoids
471 were kept in IntestiCult Organoid Growth Medium (STEMCELL Technologies) with 100 μg/ml
472 Penicillin-Streptomycin for further amplification and maintenance.

473

Organoid preparation for time-course experiments

474

475 WT organoids passage 10 were collected 5-7 days after passaging and digested with TrypLE
476 (Thermo Fisher Scientific) for 20 min at 37 °C. The resulting dissociated cells were filtered

477　through a 30 μm cell strainer (Sysmex) and single alive cells were sorted by FACS (Becton
478　Dickinson Influx cell sorter with BD FACS Sortware 1.2.0.142, or Becton Dickinson FACSAria III
479　using BD FACSDiva Software Version 8.0.1). Forward scatter and side scatter properties were
480　used to remove cell doublets and dead cells. The collected cells were resuspended in ENR
481　medium (advanced DMEM/F-12 with 15 mM HEPES (STEM CELL Technologies) supplemented
482　with 100 μg/ml Penicillin-Streptomycin, 1×Glutamax (Thermo Fisher Scientific), 1×B27
483　(Thermo Fisher Scientific), 1xN2 (Thermo Fisher Scientific), 1mM N-acetylcysteine (Sigma),
484　500ng/ml R-Spondin (kind gift from Novartis), 100 ng/ml Noggin (PeproTech) and 100 ng/ml
485　murine EGF (R&D Systems) and mixed 1:1 with Matrigel (Corning). Cells were seeded at a
486　density of 3000 cells per 5ul drops per well of 96 well imaging plates (Greiner, 655090)(2
487　plates and 3 wells per condition). After 20 min of solidification at 37 °C, 100 μl of medium was
488　overlaid. From day 0 to day 1, ENR was supplemented with 20% Wnt3a-conditioned medium
489　(Wnt3a-CM), 10 μM Y-27632 (ROCK inhibitor, STEMCELL Technologies) and 3 μM of
490　CHIR99021 (GSK3B inhibitor, STEMCELL Technologies, cat # 72054). From day 1 to 3 ENR was
491　supplemented with 20% Wnt3a-CM and 10 μM Y-27632.

492

493　Fixed sample preparation and time-course imaging

494　Organoids are embedded in a Matrigel droplet. Due to the nature of the droplet, individual
495　organoids are located at different heights in the Matrigel drop. To allow imaging of all
496　organoids within a similar z-range, each 96-well plate was centrifuged at 847 g for 10 min in
497　a pre-cooled centrifuge at 10 °C prior to fixation. Organoids were fixed in 4% PFA (Electron
498　Microscopy Sciences) in PBS for 45 min at room temperature. For time course and compound
499　experiments, organoids were permeabilized with 0.5% Triton X-100 (Sigma-Aldrich) for 1 h
500　and blocked with 3% Donkey Serum (Sigma-Aldrich) in PBS with 0.1% Triton X-100 for 1 h.

501

502　WT imaging

503　For the images in Figure 5e, membrane staining with E-Cadherin (BD Biosciences, # 610182)
504　was done at 1:300 ratio in Blocking buffer for 20 hours at 4°C. DAPI staining was performed
505　at concentration of 300 nM for 30 min at room temperature. All secondary antibodies were
506　added at 1:300 for 1 hour in room temperature. Cell nuclei were stained with 20 μg/ml DAPI
507　(4',6-Diamidino-2- Phenylindole, Invitrogen) in PBS for 15 min. High-throughput imaging was
508　done with an automated spinning disk microscope from Yokogawa (CellVoyager 7000S), with
509　an enhanced CSU-W1 spinning disk (Microlens-enhanced dual Nipkow disk confocal scanner),
510　a 40x (NA = 0.95) Olympus objective, and a Neo sCMOS camera (Andor, 2,560 × 2,160 pixels).
511　For imaging, an intelligent imaging approach was used in the Yokogawa CV7000 (Search First
512　module of Wako software). For each well, one field was acquired with 2x resolution in order
513　to cover the complete well. This overview fields were then used to segment individual
514　organoids on the fly with a custom written ImageJ macro which outputs coordinates of
515　individual organoid positions. These coordinated were then subsequently imaged with high
516　resolution (40x, NA = 0.95). For each site, z-planes spanning a range up to 140 μm were
517　acquired. For the data in Figure 5e,h and in Supplementary Figure 9 2 μm z-steps were used.

518

519 ## Lats-DKO

520 Analysed data stems from a previous publication[6], with Lats DKO organoids dissociated into
521 single cells and plated into 96 well plates, fixed and stained with DAPI following the published
522 protocols. Tamoxifen induction (1:1000) was kept in the medium until fixation time.

523

524 ## RXRi

525 RXR inhibition was achieved by adding the Cpd2170 RXR antagonist[7] compound at 1:2000
526 ratio to the medium from the moment single cells were seeded onto the light-sheet holder.
527 The compound was kept throughout the data acquisition. Organoids used for this experiment
528 had been infected with H2B-iRFP670 for live nuclei labeling.

529

530 ## Inhibition experiments: Lats1/2 and Limk1 inhibition time-course

531 For the evaluation of binucleated cells in Fig5h-i and Supplementary Figure 9, FACS sorted
532 (Becton Dickinson Influx cell sorter with BD FACS Sortware 1.2.0.142, or Becton Dickinson
533 FACSAria III using BD FACSDiva Software Version 8.0.1). WT mouse intestinal organoids at
534 passage 10 were dissociated and grown from single cells as described above. Inhibitors were
535 resuspended in DMSO and serially diluted in medium to their final working concentration and
536 added on day 0 (Lats1/2 inhibitor Truli[40] (CSNpharm, # CSN26140) or the Limk1 inhibitor
537 Damnacanthal[41] (Tocris, # 1936)). One plate was fixed with 4% PFA on day 2 (48hrs after
538 plating) and the other one on day 3 (72hrs after plating) as described in the previous section.
539 At the end of the time course all plates were permeabilized with 0.5% Triton X-100 (Sigma-
540 Aldrich) for 1 h and blocked with 3% Donkey Serum (Sigma-Aldrich) in PBS with 0.1% Triton
541 X-100 for 1 h. Primary antibodies were diluted in blocking as follow: anti- e-Cadherin (BD
542 Biosciences, # 610182) 1:400, anti-Limk1 (Abcam, # ab194798) 1:400 and anti-Yap1 (Cell
543 Signaling, # 14074) 1:400 and incubated for 1h at RT on a shaking plate. The primary
544 antibodies were washed with PBS 3x10min at RT on a shaking plate. Both secondary
545 antibodies (Alexa Fluor 568 donkey anti mouse, Thermo Fisher Scientific; A10042 and Alexa
546 Fluor 488 donkey anti rabbit, Thermo Fisher Scientific; A-21202) were diluted 1:400 and
547 incubated for 2hrs at RT on a shaking plate. The plates were then washed with PBS 3x10min
548 at RT on a shaking plate and cell nuclei were stained with 20 μg/ml DAPI (4',6-Diamidino-2-
549 Phenylindole, Invitrogen) in PBS for 15 min. Plates were then covered in aluminum foil and
550 imaged with the ImageXpress from MolecularDevices. Stacks were acquired with 20X
551 objective (0.3417 μm in X and Y) and 3 μm steps. For analysis, 200 randomly picked organoids
552 were selected for each condition and the number of binucleated cells present on each one
553 evaluated.

554

555

556 ## Light-sheet sample preparation

557 H2b-mCherry / mem9-GFP and H2B-iRFP670 organoids were collected and digested with
558 TrypLE (Thermo Fisher Scientific) for 20 min at 37 °C. Alive double positive (mCherry/GFP)
559 cells were sorted by FACS (Becton Dickinson Influx cell sorter with BD FACS Sortware
560 1.2.0.142, or Becton Dickinson FACSAria III using BD FACSDiva Software Version 8.0.1). and
561 collected in medium containing advanced DMEM/F-12 with 15 mM HEPES (STEM CELL

562 Technologies) supplemented with 100 µg/ml Penicillin-Streptomycin, 1×Glutamax (Thermo
563 Fisher Scientific), 1×B27 (Thermo Fisher Scientific), 1xN2 (Thermo Fisher Scientific), 1mM N-
564 acetylcysteine (Sigma), 500ng/ml R-Spondin (kind gift from Novartis), 100 ng/ml Noggin
565 (PeproTech) and 100 ng/ml murine EGF (R&D Systems). 2500 cells were then embedded in
566 5ul drop of Matrigel/medium in 60/40 ratio. Drops were placed in the imaging chamber and
567 incubated for 20 min before being covered with 1ml of medium. For the first three days,
568 medium was supplemented with 20% Wnt3a-CM and 10 µM Y-27632 (ROCK inhibitor,
569 STEMCELL Technologies). For the first day, in addition, 3µM of CHIR99021 (STEMCELL
570 Technologies) were supplemented. After 2 hours incubation in a cell culture incubator the
571 imaging chamber was transferred to the microscope kept at 37C and 5% CO_2.

572

573 Light-sheet imaging

574 For all light-sheet experiments a LS1-Live dual illumination and inverted detection microscope
575 from Viventis Microscopy Sàrl was used. Different single cells were selected as starting
576 positions and imaged every 10 min for up to 5 days. A volume of 150 -200µm was acquired
577 with a Z spacing of 2µm between slices and 100 ms exposure time for each slice. Laser
578 intensity was kept to a minimum necessary to still obtain reasonable signal to noise from the
579 raw data, while keeping phototoxicity to a minimum possible. Medium was exchanged
580 manually under the microscopy every day.

581

582 Fixation on time-lapse recordings

583 Organoids are embedded in 5 µm Matrigel droplets which are deposited at equal distances
584 on top of the FEP foil of the light-sheet sample holder. After live imaging is done, the medium
585 is replaced by 4% PFA in PBS, and left in the chamber for maximum 30 minutes at 37°C in the
586 microscope. After fixation the organoids were permeabilized with 0.5% Triton X-100 (Sigma-
587 Aldrich) for 1 h and blocked with 3% Donkey Serum (Sigma-Aldrich) in PBS with 0.1% Triton
588 X-100 for 1 h. For the images in Figure 4, the cyst was stained with DLL1 antibody (R&D
589 Systems, # AF3970) at 1:100 ratio and left overnight at 4°C. For Lysozyme (Dako, # A0099) we
590 used a 1:400 ratio for 3 hours at room temperature.

591

592 Registration for back-tracking after fixation of time-lapses

593 Since PFA fixation causes the Matrigel droplet to flatten, we perform imaging while fixation
594 is taking place. Typically we observe no change within the first 5 minutes, whereas after that
595 there is a sudden increase in organoid movement towards the bottom of the sample holder.
596 To take this into account, we increased the imaging volume and step size to be able to
597 encompass a larger volume and still track the organoid. For the data in Figure 4 we increased
598 stack size from 150 µm and 2 µm step size to 300 µm at 3 µm step size. However, larger values
599 can also be used.

600 Nonetheless, the flattening of the droplet will lead the organoids to rotate or translate in
601 space. Furthermore, PFA fixation also changes the shape of tissue samples by shrinking or
602 swelling. To bridge the translational, rotational and rescaling of the organoids during fixation
603 procedures, we registered fixed organoids using Elastix v4.900 (https://elastix.lumc.nl/). Since
604 Elastix can be directly installed from the repository as pre-compiled libraries, we refrained

14

605 from embedding the registration into LSTree, and left it as a stand-alone tool. For all
606 registrations using the similarity transform, a base parameter file set for performing similarity
607 transformations was used and eventually modified so that best results could be achieved. An
608 example of the registration parameters is provided in 'Elastix_parameter_Affine.txt' file in the
609 Supplementary Software.

610

611 ## LSTree modules

612 LSTree (https://github.com/fmi-basel/LSTree) is a luigi-based workflow
613 (https://github.com/spotify/luigi) which encompasses jupyter notebooks for cropping and
614 general utilities, as well as luigi lasks for denoising, deconvolution and multiscale
615 segmentation and tree-prediction, along with feature extraction. Pre-processing steps rely
616 mostly on cropping and registration, denoising, and deconvolution steps. Deconvolution was
617 based on flowdec (https://github.com/hammerlab/flowdec). Although not part of LSTree
618 itself, improvements in the microscope software (on-the-fly LZW compression, position
619 dependent illumination alignment) were performed in collaboration with Viventis Microscopy
620 Sàrl and are now part of their current microscope software. A lzw compression python code
621 ('parallel_image_compressor.py') is available in the **Supplementary Software**.

622 Detailed information regarding pre-processing, segmentation strategies and feature
623 extraction can be found in **Supplementary Text.**

624

625 ## Software

626 For deconvolution of the images, PSFs were averaged using the PSF Distiller from Huygens
627 compute engine 20.10.1p1. For visualization of images ImageJ v.1.53h and Paraview 5.8.0
628 were used, and Elastix v4.900 was used for registration of organoids.

629

630 ## IT requirements

631 The LSTree analysis tasks have been trained and used on a workstation with following
632 specifications: 16 core Intel Xeon W-2145, 64 GB 2666MHz DDR4 RAM equipped with a Nvidia
633 Quadro RTX 6000 GPU with 24 GB VRAM and using Ubuntu 18.04.6 LTS. All code runs with
634 Nvidia cudatoolkit 10.1, and cuDNN 7.

635 Minimally, one would need 16 GB of RAM and a Tensorflow compatible GPU with at least 8
636 GB of VRAM. Since many of the steps of the pipeline run in parallel, a higher number of CPUs
637 is also desirable.

638 A step-by-step guide on installation and on how to run the example data provided can be
639 found in the repository (www.github.com/fmi-basel/LSTree).

640

641 ## Statistics & Reproducibility

642 For all experiments no statistical method was used to predetermine sample size. Sample size
643 was determined based on previous related studies in the field[11,16,27]. For long-term live
644 imaging experiments, we assumed that the amount of timepoints comprised in the 7 different
645 datasets would be sufficient to test the framework. In addition, 12 other datasets from

646   previous publication[27] were used for further challenging the analysis framework). No data
647   were excluded from the analyses. Samples were randomly assigned. Investigators were not
648   blinded to allocation during experiments and outcome assessment.

649

650 # Data Availability

651   Source data are provided with this paper. A minimum example to test LSTree is provided
652   within the repository. The light-sheet data and time-course data generated in this study have
653   been deposited in the Zenodo database under accession code 10.5281/zenodo.6828906
654   [https://zenodo.org/record/6828906][42]. Due to storage space restrictions, for source light-
655   sheet image data please contact Prisca Liberali for more information.

656

657 # Code Availability

658   LSTree can be found publicly in GitHub (https://github.com/fmi-basel/LSTree) with its latest
659   release referenced also in Zenodo (DOI: 10.5281/zenodo.6826914)[17]. All other code used in
660   this work is present in the Supplementary Software.

661

References

1   Mayr, U., Serra, D. & Liberali, P. Exploring single cells in space and time during tissue development, homeostasis and regeneration. *Development* **146**, dev176727, doi:10.1242/dev.176727 (2019).

2   Zinner, M., Lukonin, I. & Liberali, P. Design principles of tissue organisation: How single cells coordinate across scales. *Current Opinion in Cell Biology* **67**, 37-45, doi:10.1016/j.ceb.2020.07.004 (2020).

3   Xavier Da Silveira Dos Santos, A. & Liberali, P. From single cells to tissue self-organization. *The FEBS Journal* **286**, 1495-1513, doi:10.1111/febs.14694 (2019).

4   Bankaitis, E. D., Ha, A., Kuo, C. J. & Magness, S. T. Reserve Stem Cells in Intestinal Homeostasis and Injury. *Gastroenterology* **155**, 1348-1361, doi:10.1053/j.gastro.2018.08.016 (2018).

5   Sato, T. *et al.* Single Lgr5 stem cells build crypt–villus structures in vitro without a mesenchymal niche. *Nature* **459**, 262-265, doi:10.1038/nature07935 (2009).

6   Serra, D. *et al.* Self-organization and symmetry breaking in intestinal organoid development. *Nature* **569**, 66-72, doi:10.1038/s41586-019-1146-y (2019).

7   Lukonin, I. *et al.* Phenotypic landscape of intestinal organoid regeneration. *Nature* **586**, 275-280, doi:10.1038/s41586-020-2776-9 (2020).

8   Yang, Q. *et al.* Cell fate coordinates mechano-osmotic forces in intestinal crypt morphogenesis. *bioRxiv pre-print server*, doi:10.1101/2020.05.13.094359 (2020).

9   Krzic, U., Gunther, S., Saunders, T. E., Streichan, S. J. & Hufnagel, L. Multiview light-sheet microscope for rapid in toto imaging. *Nat Methods* **9**, 730-733, doi:10.1038/nmeth.2064 (2012).

10   McDole, K. *et al.* In Toto Imaging and Reconstruction of Post-Implantation Mouse Development at the Single-Cell Level. *Cell* **175**, 859-876 e833, doi:10.1016/j.cell.2018.09.031 (2018).

11   Alladin, A. *et al.* Tracking cells in epithelial acini by light sheet microscopy reveals proximity effects in breast cancer initiation. *eLife* **9**, doi:10.7554/elife.54066 (2020).

12   Maioli, V. *et al.* Time-lapse 3-D measurements of a glucose biosensor in multicellular spheroids by light sheet fluorescence microscopy in commercial 96-well plates. *Sci Rep* **6**, 37777, doi:10.1038/srep37777 (2016).

13   Renner, H. *et al.* A fully automated high-throughput workflow for 3D-based chemical screening in human midbrain organoids. *Elife* **9**, doi:10.7554/eLife.52904 (2020).

14   Eismann, B. *et al.* Automated 3D light-sheet screening with high spatiotemporal resolution reveals mitotic phenotypes. *J Cell Sci* **133**, doi:10.1242/jcs.245043 (2020).

15   Kok, R. N. U. *et al.* OrganoidTracker: Efficient cell tracking using machine learning and manual error correction. *PLOS ONE* **15**, e0240802, doi:10.1371/journal.pone.0240802 (2020).

701 16 Hof, L. *et al.* Long-term live imaging and multiscale analysis identify heterogeneity and
702   core principles of epithelial organoid morphogenesis. *BMC Biology* **19**,
703   doi:10.1186/s12915-021-00958-w (2021).

704 17 Multiscale light-sheet organoid imaging framework v. v0.2 (Zenodo / Github, 2022).

705 18 Dumortier, J. G. *et al.* Hydraulic fracturing and active coarsening position the lumen of
706   the mouse blastocyst. *Science* **365**, 465-468, doi:10.1126/science.aaw7709 (2019).

707 19 Rossi, G. *et al.* Capturing Cardiogenesis in Gastruloids. *Cell Stem Cell* **28**, 230-240.e236,
708   doi:10.1016/j.stem.2020.10.013 (2021).

709 20 Krull, A., Buchholz, T.-O. & Jug, F. Noise2Void - Learning Denoising from Single Noisy
710   Images. *arXiv pre-print server*, doi:arxiv:1811.10980 (2019).

711 21 Czech, E., Aksoy, B. A., Aksoy, P. & Hammerbacher, J. Cytokit: a single-cell analysis
712   toolkit for high dimensional fluorescent microscopy imaging. *BMC Bioinformatics* **20**,
713   doi:10.1186/s12859-019-3055-3 (2019).

714 22 Ortiz, R., De Medeiros, G., Peters, A. H. F. M., Liberali, P. & Rempfler, M.   434-443
715   (Springer International Publishing, 2020).

716 23 Ulman, V. *et al.* An objective comparison of cell-tracking algorithms. *Nature Methods*
717   **14**, 1141-1152, doi:10.1038/nmeth.4473 (2017).

718 24 Moen, E. *et al. Accurate cell tracking and lineage construction in live-cell imaging*
719   *experiments with deep learning* (Cold Spring Harbor Laboratory, 2019).

720 25 Sugawara, K., Cevrim, C. & Averof, M. *Tracking cell lineages in 3D by incremental deep*
721   *learning* (Cold Spring Harbor Laboratory, 2021).

722 26 Sugawara, K., Cevrim, C. & Averof, M. Tracking cell lineages in 3D by incremental deep
723   learning. *Elife* **11**, doi:10.7554/eLife.69380 (2022).

724 27 Strnad, P. *et al.* Inverted light-sheet microscope for imaging mouse pre-implantation
725   development. *Nature Methods* **13**, 139-142, doi:10.1038/nmeth.3690 (2016).

726 28 Klein, S., Staring, M., Murphy, K., Viergever, M. A. & Pluim, J. P. W. elastix: A Toolbox
727   for Intensity-Based Medical Image Registration. *IEEE Transactions on Medical Imaging*
728   **29**, 196-205, doi:10.1109/TMI.2009.2035616 (2010).

729 29 Shamonin, D. Fast parallel image registration on CPU and GPU for diagnostic
730   classification of Alzheimer's disease. *Frontiers in Neuroinformatics* **7**,
731   doi:10.3389/fninf.2013.00050 (2013).

732 30 Yabuta, N. *et al.* N-terminal truncation of Lats1 causes abnormal cell growth control
733   and chromosomal instability. *Journal of Cell Science* **126**, 508-520,
734   doi:10.1242/jcs.113431 (2013).

735 31 Yang, X. *et al.* LATS1 tumour suppressor affects cytokinesis by inhibiting LIMK1. *Nature*
736   *Cell Biology* **6**, 609-617, doi:10.1038/ncb1140 (2004).

737 32 Lens, S. M. A. & Medema, R. H. Cytokinesis defects and cancer. *Nature Reviews Cancer*
738   **19**, 32-45, doi:10.1038/s41568-018-0084-6 (2019).

739 33 Hong, A. W., Meng, Z. & Guan, K. L. The Hippo pathway in intestinal regeneration and
740   disease. *Nat Rev Gastroenterol Hepatol* **13**, 324-337, doi:10.1038/nrgastro.2016.59
741   (2016).

742 34 Li, Q. *et al.* Lats1/2 Sustain Intestinal Stem Cells and Wnt Activation through TEAD-
743   Dependent and Independent Transcription. *Cell Stem Cell* **26**, 675-692 e678,
744   doi:10.1016/j.stem.2020.03.002 (2020).

745 35 Wheat, J. C. *et al.* Single-molecule imaging of transcription dynamics in somatic stem
746   cells. *Nature* **583**, 431-436, doi:10.1038/s41586-020-2432-4 (2020).

747 36 Losick, Vicki P., Fox, Donald T. & Spradling, Allan C. Polyploidization and Cell Fusion
748   Contribute to Wound Healing in the Adult Drosophila Epithelium. *Current
749   Biology* **23**, 2224-2232, doi:10.1016/j.cub.2013.09.029 (2013).

750 37 Zhang, S. *et al.* The Polyploid State Plays a Tumor-Suppressive Role in the Liver.
751   *Developmental Cell* **44**, 447-459.e445, doi:10.1016/j.devcel.2018.01.010 (2018).

752 38 Margall-Ducos, G., Celton-Morizur, S., Couton, D., Bregerie, O. & Desdouets, C. Liver
753   tetraploidization is controlled by a new process of incomplete cytokinesis. **120**, 3633-
754   3639, doi:10.1242/jcs.016907 (2007).

755 39 Gregorieff, A., Liu, Y., Inanlou, M. R., Khomchuk, Y. & Wrana, J. L. Yap-dependent
756   reprogramming of Lgr5+ stem cells drives intestinal regeneration and cancer. *Nature*
757   **526**, 715-718, doi:10.1038/nature15382 (2015).

758 40 Kastan, N. *et al.* Small-molecule inhibition of Lats kinases may promote Yap-
759   dependent proliferation in postmitotic mammalian tissues. *Nat Commun* **12**, 3100,
760   doi:10.1038/s41467-021-23395-3 (2021).

761 41 Ohashi, K. *et al.* Damnacanthal, an effective inhibitor of LIM-kinase, inhibits cell
762   migration and invasion. *Mol Biol Cell* **25**, 828-840, doi:10.1091/mbc.E13-09-0540
763   (2014).

764 42 de Medeiros, G., Ortiz, Raphael, Strnad, Petr, Boni, Andrea, Moos, Franziska, Repina,
765   Nicole, Chalet-Meylan, Ludivine, Maurer, Francisca, & Liberali, Prisca.   (Zenodo,
766   2022).

767

768

Acknowledgements

777 to P.L.). This work received funding from the ERC under the European Union's Horizon 2020
778 research and innovation programme (grant agreement no. 758617).

779

780

Author contributions

782 P.L. and G.M. conceived and P.L. supervised the study, P.L., G.M., and A.B. designed the
783 experiments, F.Ma., L.C.M. and G.M. cultured the organoids, G.M. and A.B. recorded the
784 time-lapses, N.R. and G.M performed backtracking experiments. F.Mo. trained and evaluated
785 tracking predictions with Elephant. P.S. wrote and implemented compression and position
786 dependent illumination code into microscope software, A.B. created first Mastodon trees, R.O.
787 wrote first LSTree workflow with the support of G.M., G.M. and L.C.M. performed time-
788 course experiments. G.M., R.O. and P.L. analysed the data from the time-lapses, G.M, L.C.M.
789 and P.L. analysed the time-course experiments, G.M., R.O. and P.L. wrote the paper.

790 Correspondence should be sent to Prisca Liberali (prisca.liberali@fmi.ch).

791

Competing Interests

793 The authors declare the following competing interests: A.B. and P.S. are co-founders of
794 Viventis Microscopy Sàrl that commercializes the light-sheet microscope used in this study.
795 The remaining authors declare no competing interests.
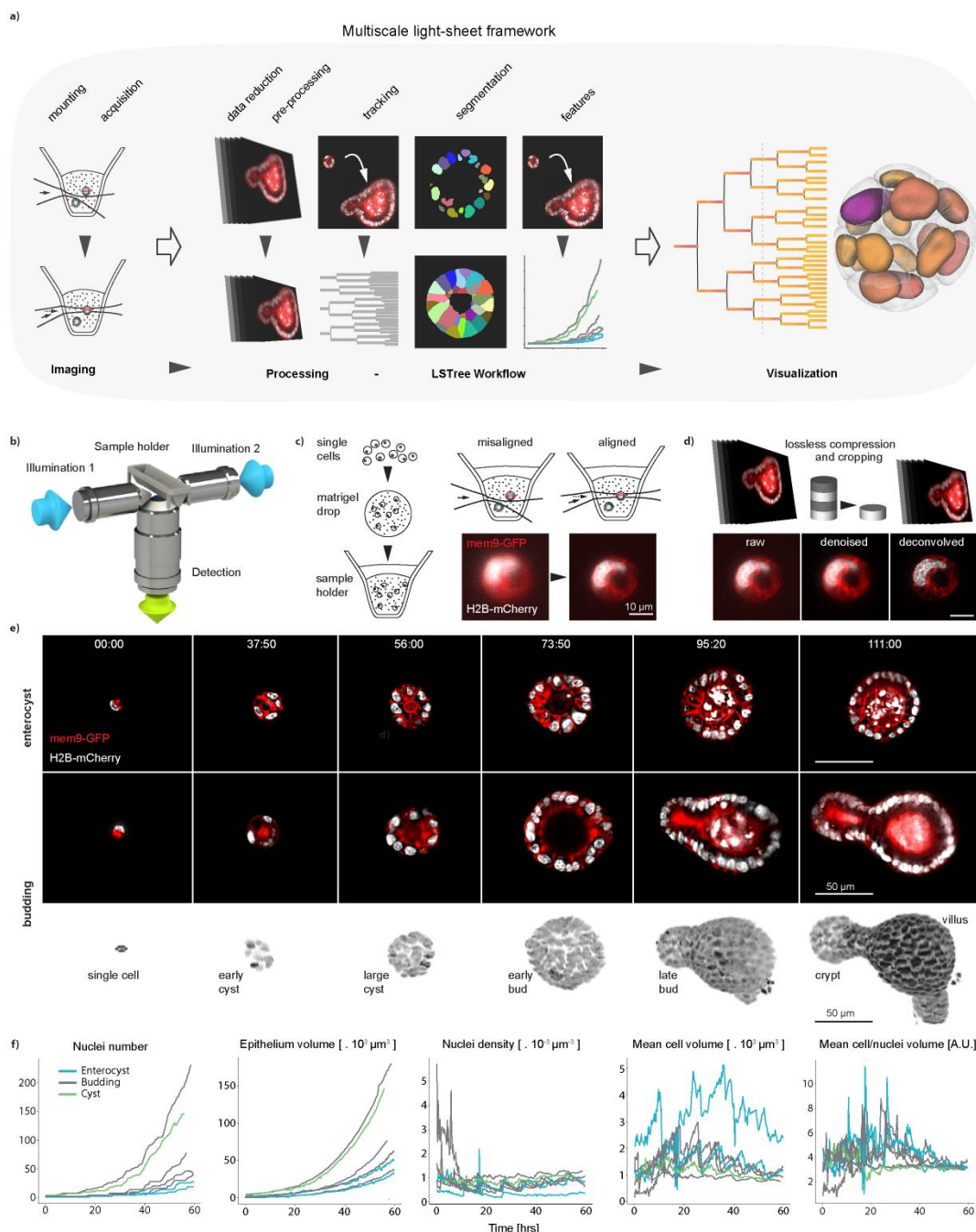
796

797

798

799

800

801

802

Figures


Figure 1: Acquisition of high-resolution 3D organoid images. a) Multiscale light-sheet imaging framework, depicting imaging stages, analysis workflow and visualization tool. **b)** Dual illumination inverted detection light-sheet objective configuration used in all of the recordings. **c)** Left: sample preparation is performed by mixing single cells dissociated from mature organoids with matrigel and depositing 5 uL drops on the light-sheet sample holder. Right: sample position dependent illumination alignment corrects for possible misalignments of the illumination beam in reaching organoids distributed inside the Matrigel drop, improving SNR. **d)** Upper row: minimization of storage needs done with on-the-fly

814   compression and further cropping steps. Lower row: denoising and deconvolution steps
815   further improve image quality. **e)** Time-lapse imaging of organoid growth. Top row shows still
816   images of a growing enterocyst, whereas both lower rows show a stereotypical growth of a
817   budding organoid as a cross sections as well as a projection in Paraview. **f)** Temporal evolution
818   of nuclei number, epithelium volume, mean cell volume and the ratio between mean cell and
819   mean nuclei volumes for all main 7 datasets considered in this work. Source data are provided
820   as a Source Data file.

821
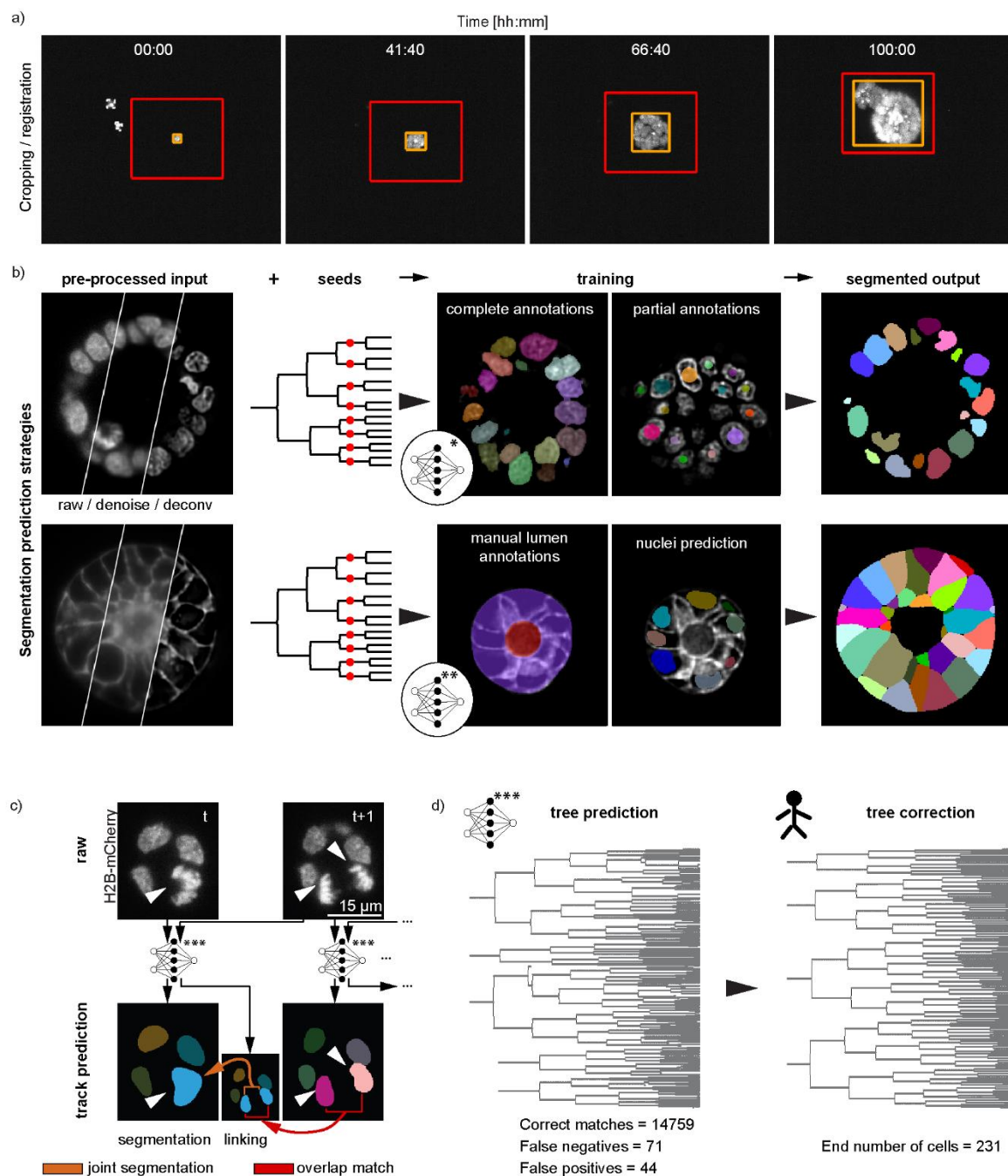
Figure 2: Cropping, segmentation and tree-prediction strategies underlying LSTree. **a)** Cropping of datasets is done in a semi-automatic way: selected object of interest is fitted with an orange (best fit for each particular timepoint) and a global red bounding boxes, which can be corrected in 3D. **b)** Nuclei and cell segmentation strategies. Upper row: denoised and deconvolved input data together with seeds from respective tracking are used as input into the network to predict nuclei volume. The network is trained with both complete and partial annotations. Lower row: Cell volume prediction follows similar input as for nuclei. Main difference is that this second network is trained with supervision of complete manual annotations of lumen and organoid along with the previously done nuclei predictions themselves. **c)** Strategy for prediction of lineage trees. Track predictions are done with each consecutive pair of frames. Each pair of frames enter the neural network and produce both the timepoint in question and a linking frame which is used to connect to the next timepoint

23

835 via overlap match. Linking itself is done via joint segmentation. **d)** Example of predicted and
836 corrected tree from a budding organoid dataset with the recording starting from two cells
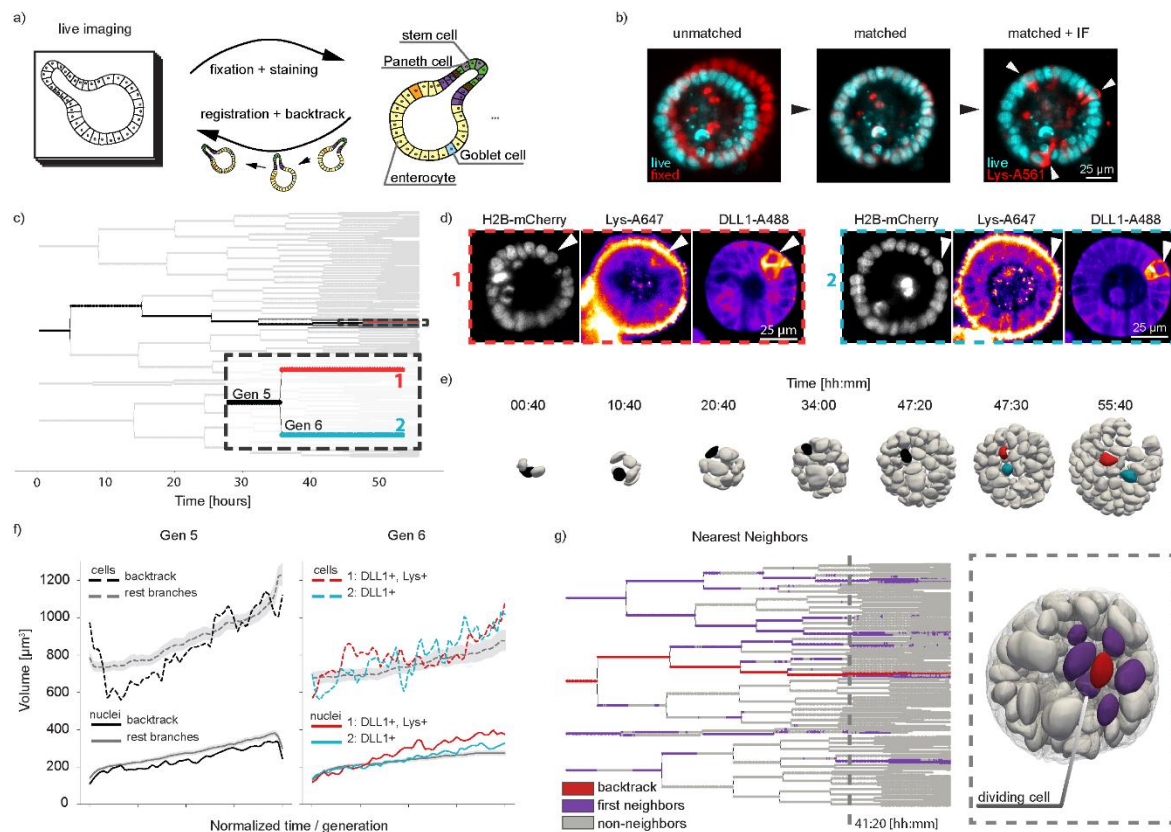837 (recording 006).
838
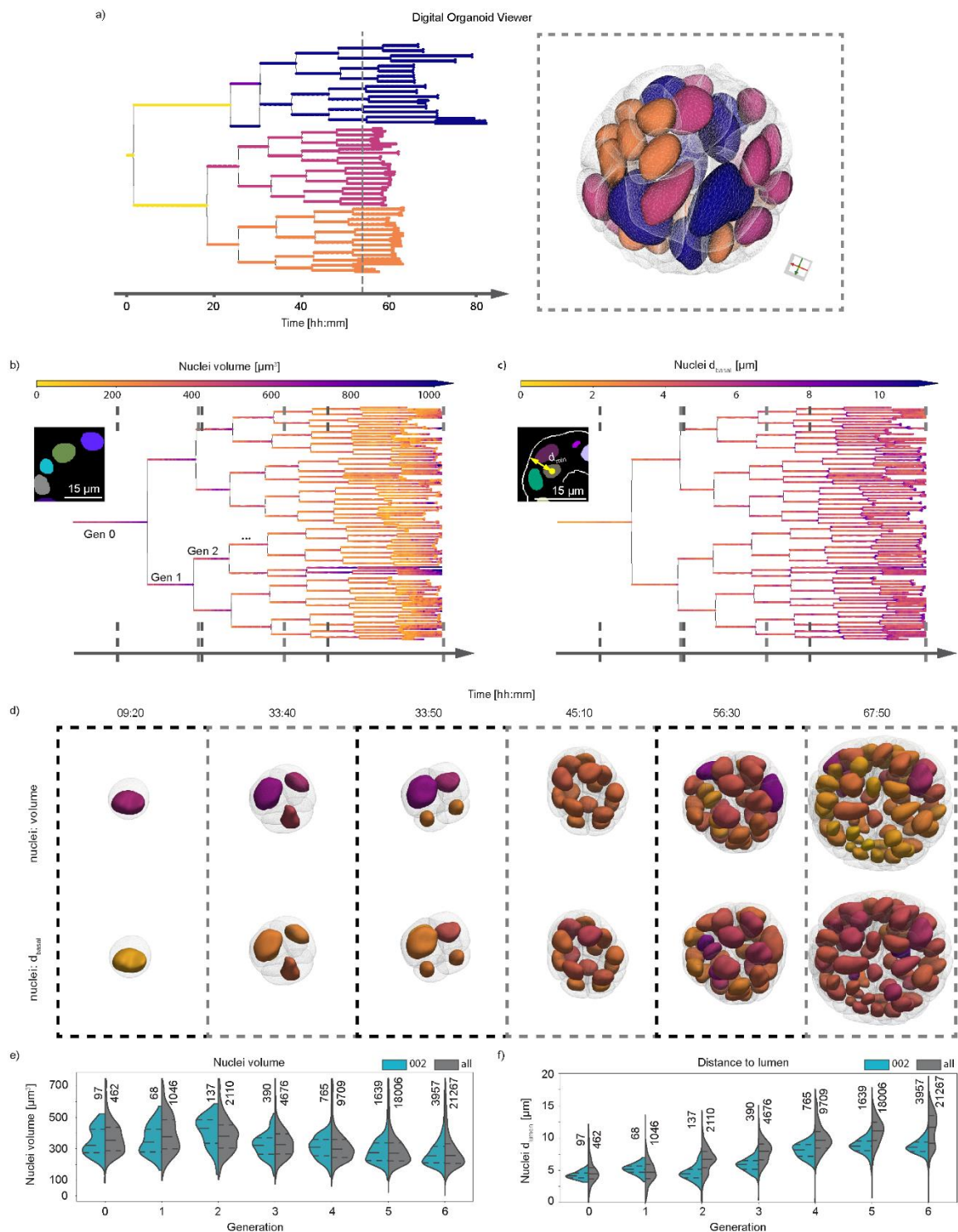
839
840 **Figure 3: Digital Organoid Viewer. a)** Digital organoid viewer is a web-based tool that shows
841 both lineage trees (left) and respective segmented nuclei and cell meshes (right)
842 simultaneously. Color coding of of each data representation can be done in a combined or
843 complementary manner. Here depicted is a color coding based on generation 2, with each of
844 the four cells acquiring different colors being propagated further in time. **b)** Overlay of the
845 nuclei segmentation as predicted in onto the lineage tree. **c)** Overlay of distance to basal
846 membrane onto the lineage tree. **d)** Visualization of the calculated meshes from nuclei and
847 cell segmentations, overlaying the corresponding values (with corresponding color map) of
848 the features presented in b) and c). The time points chosen are shown via dashed lines on

25

849   each tree in b) and c). **e,f)** Extracted values for nuclei volume **(e)** and for distance to apical
850   membrane **(f)** of the here exemplified dataset (pull, recording 002) against all datasets (all 7
851   recordings) analyzed. The dashed lines inside each plot correspond to the first and third
852   quartile of the values from all of the datasets, with the median as the dashed line in between
853   them. Each generation spans over the full cell cycle of all nuclei considered, and all nuclei
854   corresponding to each plot are shown slightly above each violinplot. Source data are provided
855   as a Source Data file.
856

857

858 **Figure 4: Fixation and backtracking after live-imaging. a)** Fixation and backtracking strategy
859 for light-sheet imaging of organoid growth (shown recording 007). **b)** After fixation a
860 registration step may be needed to overlap the fixed nuclei with the nuclei as shown in the
861 last timepoint of the timelapse. Left: midplane of raw data from last time-point H2B-mCherry
862 recording (cyan) against same plane after fixation (red). Center: registration maps the fixed
863 volume into the last time-point volume. Although overlap is not perfect, it is sufficient to maps
864 each nucleus back. Right: After registration additional information from immunolabelling can
865 be overlayed onto last time-point of the live recording, and so cells of interest can be
866 backtracked. A total of 4 different experiments were performed with similar results. **c)**
867 Lineage tree depicting the backtracking of two sister cells. **d)** After fixation, staining for DLL1
868 and Lysozyme shows two cells expressing these markers. Backtracking of them is shown in a).
869 **e)** Nuclei volume distribution for the backtracked cells against all other cells per generation.
870 **f)** Evaluation of nuclei and cell volumes for the backtracked cells against all other cells during
871 generations 5 and 6, as depicted in c). For all other cells, the midline corresponds to the mean,
872 whereas the gray region is the standard distribution. **g)** Nearest neighbor evaluation of the
873 backtracked Lys+ cell (red). All nearest neighbors are depicting in magenta, with all remaining
874 cells in gray. Dashed line on the lineage tree is presented as corresponding segmented meshes
875 on the right. A dividing cell can be recognized by the interkinetic movement of its nucleus
876 further apically. Source data are provided as a Source Data file.

877

878

879
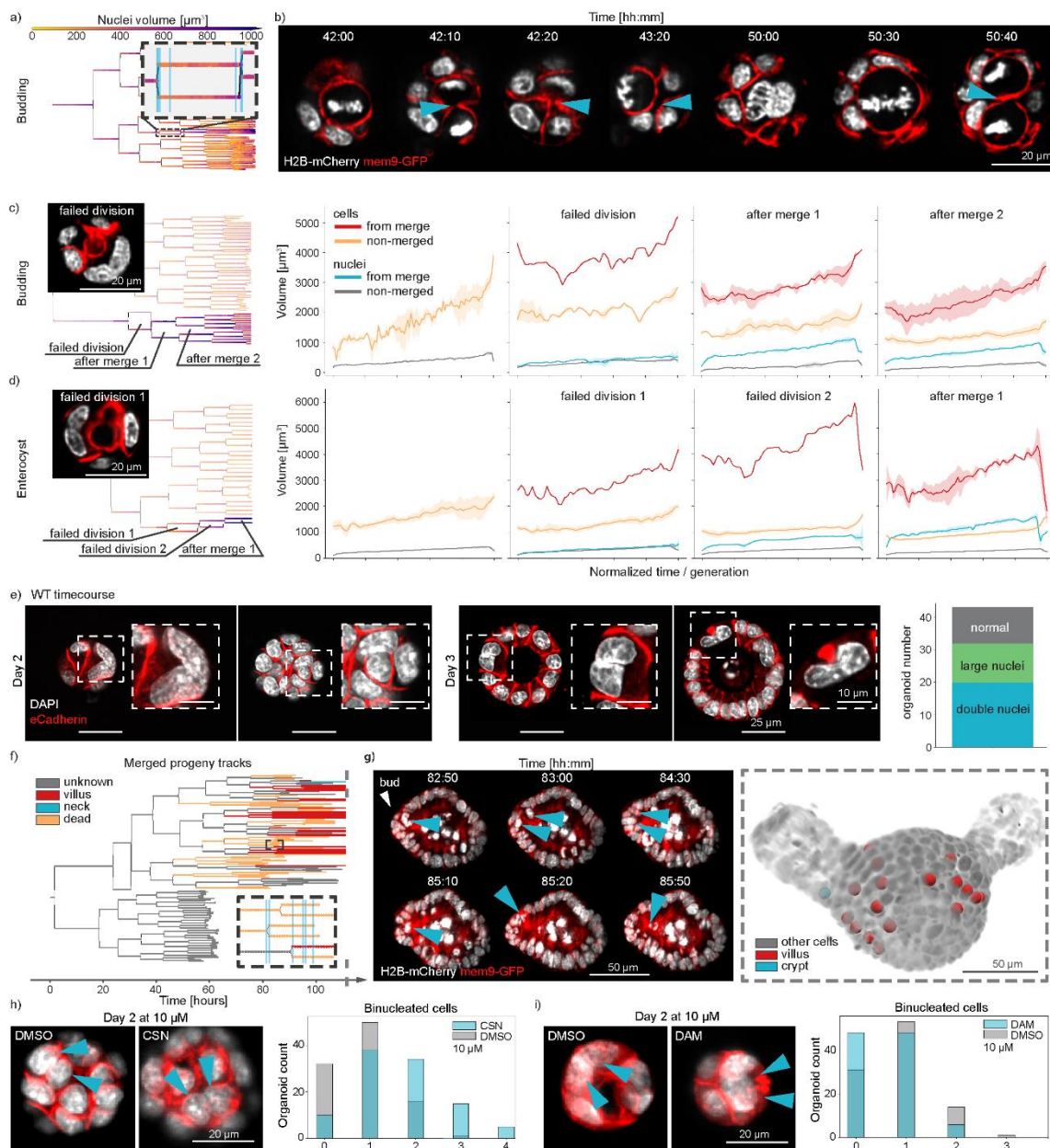
Figure 5: Merging events during early organoid growth. a) Example lineage tree with highlighted insert depicting a cell division where two nuclei divide again into two nuclei (recording 002). **b)** Still images of the light-sheet recording related to the dataset in a). Cyan arrows mark the position of a connecting region between the two nuclei until the following division occurs, where cytokinesis is successful. Corresponding locations for each depicted timepoint on the lineage tree are shown as cyan lines in the insert in a). **c,d)** Examples of different sequence of events following a failed division during budding organoid (recording 001) and enterocyst (recording 003) growth (left),with quantified nuclei and cell volumes for the highlighted events on the trees (right). Whenever more than one track is being evaluated for the same label, the full line represents the mean whereas the shaded region corresponds to 95% of the confidence interval. **e)** Timecourse data on wild-type intestinal organoids grown from single cells and fixed at days 2 and 3 after seeding. Staining with DAPI and e-Cadherin show binucleated cells and cells with large nuclei. Major axis length of all nuclei after a failed division (green) and all other cells (gray)shown on the right. **f)** Typical outcome of progeny

28

894   from a failed division; *dead* tracks end with nuclei inside the lumen or basally extruded,
895   unknown corresponds to tracks where the high level of cell packing and/or the low quality of
896   the images made it impossible to continue and know their fate, and *alive* corresponds to
897   tracks where the cells are still part of the epithelium until the end of the recording. **g)** Left:
898   still images depicting timepoints highlighted in the inset in f), with nuclei ending in the lumen.
899   Right: overlay of tracked cells from left panel onto the last time-point of the recording,
900   showing the spatial organization of the cells in the crypt and vilus regions (recording 001). **h,i,**
901   **left panel)** Example images of binucleated cells for both control and compound treated
902   organoids, with nuclei highlighted via the arrows. **h,i, right panel)** Organoid count with
903   specific number of binucleated cells for control (DMSO) and compound treated cases. 200
904   organoids have been randomly selected for evaluation on each case. Source data are provided
905   as a Source Data file.
906